Origin of spatial variation in United States East Coast sea level trends during 1900–2017

Christopher G. Piecuch[1], Peter Huybers[2], Carling C. Hay[3], Andrew C. Kemp[4], Christopher M. Little[5], Jerry X. Mitrovica[2], Rui M. Ponte[5], & Martin P. Tingley[6]

[1] *Woods Hole Oceanographic Institution, Woods Hole, Massachusetts, USA*

[2] *Harvard University, Cambridge, Massachusetts, USA*

[3] *Boston College, Boston, Massachusetts, USA*

[4] *Tufts University, Medford, Massachusetts, USA*

[5] *Atmospheric and Environmental Research, Inc., Lexington, Massachusetts, USA*

[6] *Los Gatos, California, USA*

Identifying the causes of historical trends in relative sea level—the height of the sea surface relative to Earth's crust—is a prerequisite for predicting future changes. Rates of change along the U.S. East Coast during the last century were spatially variable, and relative sea level rose faster along the Mid-Atlantic Bight than the South Atlantic Bight and Gulf of Maine. Past studies suggest that Earth's ongoing response to the last deglaciation[1–5], surface redistribution of ice and water [5–9], and changes in ocean circulation[9–13] contributed importantly to this large-scale spatial pattern. Here we analyze instrumental data[14,15] and proxy reconstructions[4,12] using probabilistic methods[16–18] to show that vertical motions of Earth's crust exerted the dominant control on regional spatial differences in relative sea level trends along the U.S. East Coast during 1900–2017, explaining a majority of the large-scale spatial

variance. Rates of coastal subsidence caused by ongoing relaxation of the peripheral forebulge associated with the last deglaciation are strongest near North Carolina, Maryland, and Virginia. Such structure indicates that Earth's elastic lithosphere is thicker than has been assumed in other models[19–22]. We also find a significant coastal gradient in relative sea level trends over this period that is unrelated to deglaciation, and suggests contributions from twentieth-century redistribution of ice and water. Our results indicate that the majority of large-scale spatial variation in longterm rates of relative sea level rise on the U.S. East Coast was due to geological processes that will persist at similar rates for centuries into the future.

Relative sea level (RSL) is the distance separating Earth's crust from the sea surface. Changes in RSL can arise from any number of geological processes or climate dynamics that impact vertical land motion (VLM), sea surface height (SSH), or both. Identifying the processes responsible for RSL changes in historical coastal tide gauge records is important for anticipating future coastal hazards and constraining recent global-mean RSL rise[6,7,22,23].

A longstanding puzzle has been the origin of large-scale spatial variation in centennial RSL trends as measured by tide gauges along the U.S. East Coast[1–13,24] (Extended Data Fig. 1), which are higher along the Mid-Atlantic Bight than the South Atlantic Bight and Gulf of Maine (Fig. 1a). Earlier studies argue that vertical crustal motions and gravity field changes tied to glacial isostatic adjustment (GIA)—Earth's ongoing viscoelastic adjustment to the termination of the last ice age—are the dominant contributors to the spatial variation in RSL trends[1,2], such that higher trends on the Mid-Atlantic Bight reflect ongoing subsidence of the peripheral forebulge of the Laurentide Ice

Sheet. Noting discrepancies between patterns of coastal RSL trends inferred from GIA models and tide gauge data, however, other work has highlighted the importance of ocean dynamics[10], tectonic motions[24], or errors in GIA models[3]. More recently, investigations using updated GIA models, proxy reconstructions derived from saltmarsh sediment, and Global Positioning System (GPS) data hypothesize that, in addition to GIA, sediment compaction[5,6], dam retention[7,8], groundwater withdrawal[7,8], melting of the Greenland Ice Sheet[9], ocean thermal expansion[9,13], or changes in ocean circulation[10–12] contribute to the spatial variation in U.S. East Coast RSL trends.

It is unclear whether these studies are contradictory. Formal error bars provided in these various studies do not account for important uncertainties inherent to the models, data, and processes under consideration. Models of GIA suffer from uncertainties tied to ice history, mantle viscosity, and lithospheric thickness[3]. Point-referenced tide gauge records, GPS data, and saltmarsh-sediment proxy reconstructions can be short, sparse, and fragmented; contaminated by local noise; and are seldom co-located alongside one another[17,25] (e.g., Fig. 1a, 1b). Further complicating interpretation of differences among studies is the existence of dependencies between models and data, and between different datasets, which have been ignored[16]. Rigorously determining the relative roles of VLM and SSH changes, and the sufficiency of GIA in explaining the observed large-scale spatial structure in U.S. East Coast RSL trends, requires a mathematically coherent synthesis of available observations and models.

We use Bayesian data analysis[16–18] to jointly infer the large-scale ($\gtrsim 500$ km) spatial structure of centennial RSL trends on the U.S. East Coast during 1900–2017. The contributions of

VLM and SSH changes arising from GIA and other processes are determined at a common set of $0.5° \times 0.5°$ regularly spaced coastal grid points (see Methods). Inferences are based on 53 annual tide gauge RSL records[14], VLM estimates from 42 GPS stations[15], proxy RSL reconstructions derived from radiocarbon-dated sediment from 23 saltmarshes[4,9,12], and 216 prior GIA model predictions based on 3 ice history models[19–21] and 72 combinations of viscoelastic Earth structure parameters[23] (see Methods). RSL and other quantities of interest are modeled as processes with spatiotemporal dependencies that are described by uncertain parameters including autocorrelation timescales, spatial ranges, and error variances. Data are represented as noisy, biased, and gappy versions of the underlying processes. We invert the model using Bayes' rule to obtain the posterior probability distribution of the processes and parameters conditional on the data and prior estimates. The fully probabilistic solution provides rigorous uncertainty estimates, and allows for estimation of subtle pathwise statistics[16], such as the probability density function associated with a spatially averaged value, the spatial variance in one process that is explained by another process, or whether a particular location features an extreme value.

Separating large-scale signals of interest from local processes and noise (see Methods; Figs. 1, 2), we find it very likely (probability $P = 0.98$) that the RSL trend averaged over the Mid-Atlantic Bight (3.4 ± 0.5 mm yr^{-1}) is larger than over the South Atlantic Bight (2.7 ± 0.6 mm yr^{-1}) and Gulf of Maine (2.2 ± 0.7 mm yr^{-1}; Fig. 1c, 1f). All $\pm$ ranges are 95% posterior credible intervals. The maximum RSL rise rate (4.5 ± 0.7 mm yr^{-1}) likely ($P = 0.75$) occurs in North Carolina or Virginia, while the minimum trend (1.3 ± 0.8 mm yr^{-1}) likely ($P = 0.86$) occurs in Florida or Maine (Fig. 1e). Similarly, it is likely ($P = 0.89$) that the average VLM rate over the Mid-Atlantic

Bight (-1.4 ± 0.4 mm yr^{-1}) reflects stronger subsidence than along the Gulf of Maine (-0.1 ± 0.6 mm yr^{-1}) and South Atlantic Bight (-1.1 ± 0.5 mm yr^{-1}; Fig. 1d, 1h). Note that negative VLM reflects subsidence and, hence, contributes to sea level rise. Correspondingly, the most negative VLM rate (-2.5 ± 0.6 mm yr^{-1}) likely ($P = 0.75$) occurs in the same states hosting maximum sea level rise, North Carolina or Virginia, whereas the most positive rate of VLM (0.7 ± 0.8 mm yr^{-1}) very likely ($P = 0.90$) occurs in Maine (Fig. 1g). These regional spatial patterns are hinted at in the data (Fig. 1a, 1b), but the model solutions are considerably smoother, due to the suppression of noise associated with the spatiotemporal filtering and joint assimilation of data streams involved in the Bayesian algorithm.

There is a striking visual correspondence between the latitudinal structures of the large-scale RSL and VLM trends (Fig. 2a, 2b). Adding posterior draws of regional RSL and VLM trends decreases the alongshore variance in the latter by a median of 73% (Fig. 3). Inferred regional SSH trends are comparatively more uniform (Fig. 2c). Nevertheless, there are hints of large-scale spatial structure, such that regional SSH trends are higher north of Cape Hatteras compared to south (Fig. 2c).

More insight is gained by partitioning the regional trends (Fig. 2a–2c) into GIA and other contributions (Fig. 2d–2i; see Methods). We ascribe 69% of the large-scale variance in coastal VLM rates to GIA (median estimate). Estimated subsidence rates due to GIA are pronounced over the coastal Mid-Atlantic Bight, with the strongest trend (-1.4 ± 1.2 mm yr^{-1}) likely ($P = 0.81$) found in North Carolina, Maryland, or Virginia, reflecting collapse of the peripheral forebulge

(Fig. 2e). Large-scale SSH trends due to GIA exhibit a statistically significant ($P > 0.99$) latitudinal gradient, with values increasing from south to north (Fig. 2f)—a consequence of geoid changes associated with mantle material flowing back to areas formerly overlain by the Laurentide Ice Sheet. The maximum RSL trend due to GIA (2.0 ± 0.4 mm yr^{-1}) is likely ($P = 0.69$) found in North Carolina, Maryland, or Virginia, but unlikely ($P = 0.23$) found in the states of Delaware or New Jersey, which are further north. This contrasts with past analyses of saltmarsh-sediment proxy reconstructions reasoning that the maximum rate of late-Holocene and ongoing RSL rise on the U.S. East Coast due to relaxation of the peripheral forebulge is found in Delaware or New Jersey[4]. This apparent discrepancy arises from the uneven spatial distribution of the available saltmarsh reconstructions (see Supplementary Information).

Posterior GIA estimates are narrower than their corresponding priors (Fig. 2e, 2f), indicating that the posterior solutions are informative for distinguishing between the uncertain Earth structures and ice histories. Depending on ice and Earth-model choice, root-mean-square deviations between prior predictions and posterior solutions for RSL trends due to GIA are 0.4–1.9 mm yr^{-1} (95% credible interval; e.g., Fig. 4a). Viscosity ranges of $0.3–0.5 \times 10^{21}$ Pa s and $2–3 \times 10^{21}$ Pa s for the upper and lower mantle are, respectively, very likely ($P = 0.92$; Fig. 4b), and these are consistent with a recent study[26] comparing observed elevations of sea level high stand markers along the U.S. East Coast and the Caribbean to GIA model simulations during Marine Isotope Stages 5a and 5c. Our posterior GIA solutions are mostly constrained by the saltmarsh reconstructions and GIA priors, while the instrumental records have less influence (see Supplementary Information). The ice models adopted here[19–21] were constructed by assuming an underlying viscoelastic

Earth structure, and are not independent of the Earth models. Earth models assumed in earlier studies[19–21] have viscosity structures similar to the prior Earth models favored by our posterior solutions (Fig. 4a, 4b), so the viscosity ranges quoted above may be a natural consequence of the adopted ice models. However, the elastic lithospheric thickness favored here (125 km; $P = 0.86$) is higher compared to previous works[19–22]. In keeping with physical intuition, the GIA solutions comprising our prior have a forebulge location that tends to be located more southward with thicker lithosphere.

Given the long timescales characterizing GIA, the posterior solutions can be used to project RSL rise due to GIA into the future (Fig. 4c). RSL averaged over the South Atlantic Bight, Mid-Atlantic Bight, and Gulf of Maine is predicted to rise by 2.5 ± 3.7, 10.3 ± 2.2, and 4.3 ± 2.6 cm, respectively, during 2018–2100 due to GIA (Fig. 4d). New York City and Washington, D.C. are expected to experience respective increases of 9.6 ± 4.5 and 11.0 ± 4.8 cm (Table S5), consistent with other recent estimates[5,22,27]. Such changes related to inexorable geological processes will exacerbate predicted sea level rise due to ocean thermal expansion, melting land ice, and ocean circulation changes[22,27].

While GIA is the first-order control on the regional spatial structure in centennial RSL trends, second-order contributions from other processes are evident in the posterior solution (Fig. 2g–2i). RSL trends unrelated to GIA very likely ($P = 0.95$) increase from northern Maine to southern Florida (Fig. 2g). This structure is consistent with recent work[28] suggesting that ice melting, groundwater pumping, and dam building globally since 1900 have caused higher RSL trends along the southern South Atlantic Bight compared to the northern Gulf of Maine. Regional subsidence due to groundwater pumping and sediment compaction in South Carolina, North Carolina, and New Jersey reported previously[5–7] does not feature strongly in our large-scale estimation, in that 95% credible intervals overlap zero (Fig. 2h), but residual analysis reveals significant local subsidence in these areas (see Supplementary Information). After removing the latitudinal trend, we find it very likely ($P = 0.91$) that Maine (at 43°N) is experiencing regional uplift (positive VLM) unrelated to GIA (Table S6), corroborating a recent hypothesis[8] that coastal Maine is uplifting isostatically in response to dam building over Québec, Canada. The coastal SSH expression of a poleward migration of the Gulf Stream during the twentieth century[11]—higher trends on the Mid-Atlantic Bight compared to the South Atlantic Bight and Gulf of Maine—does not appear in our posterior solution (Fig. 2i; Table S6). Furthermore, our solution is inconsistent with a dominant centennial contribution from ocean thermal expansion[13] or declining Atlantic circulation and meridional heat transport[29–31], which would lead to higher RSL and SSH trends to the north of Cape Hatteras compared to the south[32].

We identified the influences of VLM and SSH changes, arising from GIA and other processes, on the large-scale spatial variation in U.S. East Coast RSL trends during 1900–2017. These findings clarify and build upon previous studies[1–13,24]. Additional experiments demonstrate that our model solutions are robust to reasonable alternative selections for the priors on the scalar model parameters, study period duration, and GPS dataset (see Supplementary Information). This work illustrates the value of jointly assimilating disparate data streams and modeling coupled physical processes within a coherent probabilistic framework for rigorous uncertainty quantification. In future work it will be useful to consider a broader region and incorporate spatial patterns associated with different mass sources to disaggregate terrestrial water storage and land ice contributions from large-scale RSL rends (Fig. 2g).

1. Gornitz, V., & L. Seeber. Vertical crustal movements along the East Coast, North America, from historic and late Holocene sea level data, *Tectonophysics*, **178**, 127–150 (1990)

2. Peltier, W. R., & A. M. Tushingham. Influence of glacial isostatic adjustment on tide gauge measurements of secular sea level change, *J. Geophys. Res.*, **96**, B4, 6779–6796, doi:10.1029/90JB02067 (1991).

3. Davis, J. L., & J. X. Mitrovica. Glacial isostatic adjustment and the anomalous tide gauge record of eastern North America, *Nature*, **379**, 331–333 (1996).

4. Engelhart, S.E. & and B. P. Horton. Holocene sea-level database for the Atlantic coast of the United States, *Quaternary Sci. Rev.*, **54**, 12–25 (2012).

5. Kopp, R. E. Does the mid-Atlantic United States sea level acceleration hot spot reflect ocean dynamic variability? *Geophys. Res. Lett.*, **40**, 3981–3985, doi:10.1002/grl.50781 (2013).

6. Miller, K. G., R. E. Kopp, B. P. Horton, J. V. Browning, & A. C. Kemp. A geological perspective on sea-level rise and its impacts along the U.S. mid-Atlantic coast, *Earth's Future*, **1**, 3–18, doi:10.1002/2013EF000135 (2013).

7. Karegar, M. A., T. H. Dixon, & S. E. Engelhart. Subsidence along the Atlantic Coast of North America: Insights from GPS and late Holocene relative sea-level data *Geophys. Res. Lett.*, doi:10.1002/2016GL068015 (2016).

8. Karegar, M. A., T. H. Dixon, R. Malservisi, J. Kusche, & S. E. Engelhart. Nuisance Flooding and Relative Sea-Level Rise: the Importance of Present-Day Land Motion, *Sci. Rep.-UK*, **7**, 1197, doi:10.1038/s41598-017-11544-y (2017).

9. Engelhart, S. E., B. P. Horton, B. C. Douglas, W. R. Peltier, & T. E. Törnqvist. Spatial variability of late Holocene 20th century sea-level rise along the Atlantic coast of the United States, *Geology*, **37**, 12, 1115–1118, doi: 10.1130/G30360A (2009).

10. Douglas, B. C. Global sea level rise, *J. Geophys. Res.*, **96**, C4, 6981–6992, doi:10.1029/91JC00064 (1991).

11. Yin, J., & P. B. Goddard. Oceanic control of sea level rise patterns along the East Coast of the United States, *Geophys. Res. Lett.*, **40**, 5514–5520, doi:10.1002/2013GL057992 (2013).

12. Kemp, A. C., et al. Late Holocene sea- and land-level change on the U. S. Southeastern Atlantic coast, *Mar. Geol.*, **357**, 90–100 (2014).

13. Wake, L., G. Milne, & E. Leuliette. 20th Century sea-level change along the eastern US: Unravelling the contributions from steric changes, Greenland Ice Sheet mass balance and Late Pleistocene glacial loading, *Earth Planet. Sc. Lett.*, **250**, 572–580 (2006).

14. Holgate, S. J., et al. New Data Systems and Products at the Permanent Service for Mean Sea Level, *J. Coastal Res.*, **29**, 3, 493–504 (2013).

15. Santamaría-Gómez, A., et al. Uncertainty of the 20th century sea-level rise due to vertical land motion errors, *Earth Planet. Sci. Lett.*, **473**, 24–32 (2017).

16. Tingley, M. P., & P. Huybers. Recent temperature extremes at high northern latitudes unprecedented in the past 600 years, *Nature*, **496**, 201–205 (2013).

17. Piecuch, C. G., P. Huybers, & M. P. Tingley. Comparison of full and empirical Bayes approaches for inferring sea-level changes from tide-gauge data, *J. Geophys. Res. Oceans*, **122**, 2243–2258, doi:10.1002/2016JC012506 (2017).

18. Cressie, N., & C. K. Wikle. Statistics for Spatio-Temporal Data, John Wiley & Sons, 588 pp (2011).

19. Peltier, W. R. Global Glacial Isostasy and the Surface of the Ice-Age Earth: The ICE-5G (VM2) Model and GRACE, *Annu. Rev. Earth Planet. Sci.*, **32**, 111–149 (2004).

20. Peltier, W. R., D. F. Argus, & R. Drummond. Space geodesy constrains ice age terminal deglaciation: The global ICE-6G_C (VM5a) model, *J. Geophys. Res. Solid Earth*, **120**, 450–487, doi:10.1002/2014JB011176 (2015)

21. Lambeck, K., H. Rouby, A. Purcell, Y. Sun, & M. Sambridge. Sea level and global ice volumes from the Last Glacial Maximum to the Holocene, *P. Natl. Acad. Sci. USA*, **111**, 43, 15296–15303 (2014).

22. Love, R., et al. The contribution of glacial isostatic adjustment to projections of sea-level change along the Atlantic and Gulf coasts of North America, *Earth's Future*, **4**, 440–464, doi:10.1002/2016EF000363 (2016).

23. Hay, C. C., E. Morrow, R. E. Kopp, & J. X. Mitrovica. Probabilistic reanalysis of twentieth-century sea-level rise, *Nature*, **517**, 481–484, doi:10.1038/nature14093 (2015).

24. Uchipi, E., & D. G. Aubrey. Suspect Terranes in the North American Margins and Relative Sea-Levels, *J. Geol.*, **96**, 1, 79–90 (1998).

25. Wöppelmann, G., & M. Marcos. Vertical land motion as a key to understanding sea level change and variability. *Rev. Geophys.*, **54**, 64–92, doi:10.1002/2015RG000502 (2016).

26. Creveling, J. R., J. X. Mitrovica, P. U. Clark, C. Waelbroeck, & T. Pico. Predicted bounds on peak global mean sea level during marine isotope stages 5a and 5c, *Quaternary Sci. Rev.*, **163**, 193–2008 (2017).

27. Kopp, R. E., et al. Probabilistic 21st and 22nd century sea-level projections at a global network of tide-gauge sites, *Earth's Future*, **2**, 383–406, doi:10.1002/2014EF000239 (2014).

28. Hamlington, B. D., et al. Observation-driven estimation of the spatial variability of 20th century sea level rise, *J. Geophys. Res. Oceans*, **123**, 2129–2140, doi:10.1002/2017JC013486 (2018).

29. Rahmstorf, S., et al. Exceptional twentieth-century slowdown in Atlantic Ocean overturning circulation, *Nature Clim. Change*, **5**, 475–480 (2015).

30. Caesar, L., S. Rahmstorf, A. Robinson, G. Feulner, and V. Saba. Observed fingerprint of a weakening Atlantic Ocean overturning circulation, *Nature*, **556**, 191–196 (2018).

31. Thornalley, D. J. R., et al. Anomalously weak Labrador Sea convection and Atlantic overturning during the past 150 years, *Nature*, **556**, 227–230 (2018).

32. McCarthy, G. D., I. D. Haigh, J. J.-M. Hirschi, J. P. Grist, & D. A. Smeed. Ocean impact on decadal Atlantic climate variability revealed by sea-level observations, *Nature*, **521**, 508–510, doi:10.1038/nature14491 (2015).

Supplementary Information is linked to the online version of the paper at www.nature.com/nature.

Acknowledgements Funding came from Woods Hole Oceanographic Institution's Investment in Science Fund; Harvard University; NSF awards 1558939, 1558966, and 1458921; and NASA awards NNH16CT01C, NNX17AE17G, and 80NSSC17K0698. We acknowledge helpful conversations with S. Adhikari, B.D. Hamlington, F.W. Landerer, S.J. Lentz, and P.R. Thompson. Comments from three anonymous referees and the editor, Michael White, are greatly appreciated.

Author Contributions C.G.P. and P.H. jointly conceived the study. C.G.P., P.H., and M.P.T. formulated the model framework. C.C.H. and J.X.M. provided the GIA model solutions. A.C.K. provided the sea level index points. C.G.P. performed the analyses and wrote the manuscript with input from all authors.

Competing Interests The authors declare that they have no competing financial interests.

Correspondence Correspondence and requests should be addressed to C.G.P. (cpiecuch@whoi.edu).

Data Availability The tide gauge and GPS data that support the findings of this study are available from the Permanent Service for Mean Sea Level (http://www.psmsl.org/) and Système d'Observation du Niveau des Eaux Littorales (http://www.sonel.org/), respectively. The proxy reconstructions are available from published databases[4,12] and included with the model code (see Code Availability Statement). The GIA model predictions used to generate the results in this study are included with the model code (see Code Availability Statement). Maps in display items were produced using the Mapping Toolbox in MATLAB.

Code Availability Statement The computer code used to run the Bayesian model and produce the results in this study, written in the MATLAB software environment, is available at the corresponding author's GitHub website (https://github.com/christopherpiecuch).

1 Methods

Observational data We use data from 47 tide gauges on the U.S. East Coast (Table S1). Data span the South Atlantic Bight (south of Cape Hatteras), Mid-Atlantic Bight (Cape Hatteras to Cape Cod), and Gulf of Maine (north of Cape Cod). We also use 6 additional tide gauges along the southeastern Gulf of Mexico (Naples, Fort Myers, St. Petersburg) and southwestern Atlantic Canada (Saint John, Yarmouth, Halifax) to better constrain the inference at the endpoints of the domain (southern South Atlantic Bight, northern Gulf of Maine). The annually averaged time series of mean RSL were downloaded from the Permanent Service for Mean Sea Level (PSMSL) Revised Local Reference (RLR) database[14,33] on 24 May 2018. Most records have at least 25 years of valid annual values. Exceptions include shorter records along the Florida coast (e.g., Lake Worth Pier, Trident Pier, Daytona Beach), incorporated to fill a spatial gap in coverage. The dataset contains 3,248 gauge-years of data over 1900–2017 ($\sim 52\%$ completeness).

We also use vertical velocities and standard errors from 42 GPS stations on the U.S. East Coast from the Université de La Rochelle (ULR) 6a dataset[15] (Table S2). Stations feature between 3–19 years of observations over 1995–2014 with $\geq 70\%$ data completeness. Vertical velocities have been computed by researchers at ULR based on simultaneous fits of linear trends, position discontinuities, seasonal cycles, and draconitic signals to daily station position estimates, while errors have been calculated using a power law plus white noise model for the residuals[15]. Values are expressed in the 2008 realization of the International Terrestrial Reference Frame[34]. Standard errors provided with the dataset do not account for uncertainties associated with accurately realizing a stable International Terrestrial Reference Frame (e.g., related to the origin and scale factor[25]). Data were retrieved from Système d'Observation du Niveau des Eaux Littorales (SONEL) on 24 October 2017.

We also use proxy RSL reconstructions derived from radiocarbon-dated saltmarsh sediment, often called RSL index points, which are given as pairs of calibrated age and RSL (the difference between the altitude of a sample and the midpoint of its indicative range[35]). We use 164 RSL index points from 23 saltmarshes culled from the Holocene database of Engelhart and Horton[4] and updated to include data from northeastern Florida[12] (Table S3). The formal uncertainties account for indicative range, radiocarbon dating, surveying, and coring errors, but not sediment consolidation errors. The geographic distribution of the data is highly uneven along the U.S. East Coast. Because we desire to constrain contemporary trends related to GIA, we only consider RSL index points whose median calibrated age is between 2,000 and 150 years before present (where the "present" is the year 1950). For a given saltmarsh site to be considered in the analysis, it must have at least 3 RSL index points with median ages within this specified range. We select this age range to predate a dominant anthropogenic influence on RSL, and to consider a period during which the contribution of GIA to RSL trends can reasonably be approximated as linear through time.

GIA model predictions We incorporate predictions for contemporary VLM and SSH rates from 216 GIA models. Model predictions are distinguished by values used for lithospheric thickness $(72, 100, 125$ km), upper-mantle viscosity $(0.3, 0.5, 0.8, 1.0 \times 10^{21}$ Pa s), lower-mantle viscosity

$(2, 3, 5, 8, 10, 20 \times 10^{21}$ Pa s), and ice history (ICE-5G[19], ICE-6G[20], and ANU[21]). Model solutions are generated as described by Hay et al.[23] and brought into the Bayesian framework as priors, as described below and in the Supplementary Information.

Bayesian framework We develop a Bayesian algorithm for analyzing tide gauge records, GPS data, RSL index points, and GIA model predictions. The algorithm is a hierarchical dynamical spatiotemporal model[18]. The basic design follows Piecuch et al.[17], who describe an algorithm for analyzing tide gauge data on the North American Northeast Coast. Generalizations are made to analyze a larger region; to assimilate GPS data, RSL index points, and GIA model solutions; and to separate the regional signals from local noise. A residual analysis justifying the model's form given the data follows in the Supplementary Information.

Process level We desire to model RSL, VLM, and SSH due to GIA and other processes. Given the nature of the data, our approach is to distinguish two periods, during which the controls on RSL changes are expected to be different. The first period is the modern era (since 1900), during which anthropogenic forcing affects centennial RSL rise, and instrumental data are available. For this period, during which observations are precisely dated, we seek to infer RSL process at all times and locations. The second period is a pre-industrial period (between 2,000 and 150 years before present), during which geological effects are expected to have a dominant control on longterm RSL trends, and RSL index points are available. For this period, during which the RSL index points have uncertain ages, we seek to infer the RSL process only at a subset of times and locations.

First, consider the instrumental period. We model the spacetime evolution of the modern RSL process, $\boldsymbol{y}_k = [y_{1,k}, \ldots, y_{N,k}]^{\mathsf{T}}$, for time steps $k \in \{1, \ldots, K\}$ and locations $n \in \{1, \ldots, N\}$ as a spatial field of linear temporal trends superimposed on a first-order autoregressive [AR(1)] process driven by spatially correlated temporal innovations,

$$\boldsymbol{y}_k - \boldsymbol{b}t_k = r\left(\boldsymbol{y}_{k-1} - \boldsymbol{b}t_{k-1}\right) + \boldsymbol{e}_k. \tag{1}$$

Here t_k is the time at step k, r is the AR(1) coefficient, $\boldsymbol{b}$ is the spatial vector of temporal trends, and $\boldsymbol{e}_k$ is the sequence of innovations. All model parameters are listed in Table S4. The decision to model the detrended RSL residuals as an AR(1) process was motivated by the work of Bos et al.[36], who demonstrate that this assumption is justifiable for annual changes. Time steps are centered on zero, such that $\sum_{k=1}^{K} t_k = 0$. We model $\boldsymbol{e}_k$ as a zero-mean, temporally independent and identically distributed (IID), spatially correlated vector, $\boldsymbol{e}_k \sim \mathcal{N}\left(\mathbf{0}_N, \Sigma\right)$, where $\sim$ is read "is distributed as", $\mathcal{N}\left(\boldsymbol{p}, \mathsf{q}\right)$ is the multivariate normal vector distribution with mean $\boldsymbol{p}$ and covariance q, $\mathbf{0}_X$ is the $X \times 1$ column vector of zeros, and Σ is the $N \times N$ spatial covariance matrix given by,

$$\Sigma_{ij} = \left(\mathsf{c}_{ij}\right)\sigma^2 \exp\left(-\phi\left|\mathbf{s}_i - \mathbf{s}_j\right|\right). \tag{2}$$

In equation (2), σ^2 is the partial sill[37], ϕ is the inverse range, and $|\mathbf{s}_i - \mathbf{s}_j|$ is distance between locations $\mathbf{s}_i$ and $\mathbf{s}_j$. Since RSL fluctuations north of Cape Hatteras are uncorrelated with RSL variations south of Cape Hatteras[38–40], the matrix element c_{ij} equals 1 if $\mathbf{s}_i$ and $\mathbf{s}_j$ are both either north or south of Cape Hatteras (~ 35.25°N), and equals 0 otherwise.

We partition the field of RSL trends $\boldsymbol{b}$ into SSH ($\boldsymbol{w}$) and VLM ($\boldsymbol{u}$) components,

$$\boldsymbol{b} = \boldsymbol{w} - \boldsymbol{u}. \tag{3}$$

Rates of VLM and SSH are decomposed into contributions due to GIA (denoted by subscript g) and unrelated to GIA (denoted by primed superscript),

$$\begin{aligned} \boldsymbol{u} &= \boldsymbol{u}_g + \boldsymbol{u}', \\ \boldsymbol{w} &= \boldsymbol{w}_g + \boldsymbol{w}'. \end{aligned} \tag{4}$$

Trends in VLM and SSH unrelated to GIA, $\boldsymbol{u}'$ and $\boldsymbol{w}'$, are represented as Gaussian random fields with spatial structure, $\boldsymbol{u}' \sim \mathcal{N}(\alpha \mathbf{1}_N, \Omega)$ and $\boldsymbol{w}' \sim \mathcal{N}(\mu \mathbf{1}_N, \Pi)$, where $\mathbf{1}_X$ is a $X \times 1$ column vector of ones,

$$\Omega_{ij} = \omega^2 \exp\left(-\rho \left|\mathbf{s}_i - \mathbf{s}_j\right|\right), \tag{5}$$

and,

$$\Pi_{ij} = \pi^2 \exp\left(-\lambda \left|\mathbf{s}_i - \mathbf{s}_j\right|\right). \tag{6}$$

Here α and μ are spatial means, ω^2 and π^2 are partial sills, and ρ and λ are inverse ranges. Trends in VLM and SSH related to GIA, $\boldsymbol{u}_g$ and $\boldsymbol{w}_g$, are assigned prior distributions based on the 216 GIA model predictions (see Supplementary Information). The set of vectors $\{\boldsymbol{b}, \boldsymbol{u}, \boldsymbol{w}, \boldsymbol{u}_g, \boldsymbol{w}_g, \boldsymbol{u}', \boldsymbol{w}'\}$ represent large-scale, long-period contributions to the trend fields.

The full VLM process $\boldsymbol{v}$ is modeled as a Gaussian field, $\boldsymbol{v} \sim \mathcal{N}(\boldsymbol{u}, \varepsilon^2 \mathsf{I}_N)$, with mean vector equal to the spatially correlated large-scale VLM field $\boldsymbol{u}$, and a spatially uncorrelated covariance matrix. Here I_X is the $X \times X$ identity matrix and ε^2 is a nugget effect[37] parameterizing the influence of local unresolved random processes. Thus, the local component of the VLM process is $\boldsymbol{v} - \boldsymbol{u}$.

Second, consider the proxy era. We are interested in RSL at N_d spacetime points, corresponding to a subset $N_s \leq N$ of locations (N_d will be the number of RSL index points, N_s will be the number of saltmarshes). We model the spatiotemporal evolution of the pre-industrial RSL process, $\boldsymbol{Y} = [Y_1, \ldots, Y_{N_d}]^\mathsf{T}$, at times, $\boldsymbol{T} = [T_1, \ldots, T_{N_d}]^\mathsf{T}$, as a spatial field of linear temporal trends related to GIA superimposed on a random spacetime residual process,

$$\boldsymbol{Y} = \left[\sum_{i=1}^{N_d} \mathbf{e}_i \mathbf{e}_i^\mathsf{T} \mathsf{G} \left(\boldsymbol{w}_g - \boldsymbol{u}_g\right) \mathbf{e}_i^\mathsf{T}\right] \boldsymbol{T} + \mathsf{D}\boldsymbol{\iota} + \boldsymbol{f}. \tag{7}$$

Here $\boldsymbol{\iota}$ is a vector of site-specific intercepts, represented as a spatially uncorrelated normal random field, $\boldsymbol{\iota} \sim \mathcal{N}\left(\beta \mathbf{1}_{N_s}, \kappa^2 \mathsf{I}_{N_s}\right)$, with mean β and variance κ^2; $\boldsymbol{f}$ is a zero-mean, IID spacetime process, $\boldsymbol{f} \sim \mathcal{N}\left(\mathbf{0}_{N_d}, \epsilon^2 \mathsf{I}_{N_d}\right)$, with variance ϵ^2; and $\mathbf{e}_i$ is the ith standard basis function of $\mathbb{R}^{N_d}$. The matrices G and D are selection matrices of ones and zeros, which isolate the GIA-driven RSL trend $(\boldsymbol{w}_g - \boldsymbol{u}_g)$ and the intercept $(\boldsymbol{\iota})$, respectively, at the relevant target location. For example, G_{ij} equals one if element $i \in \{1, \ldots, N_d\}$ of $\boldsymbol{Y}$ corresponds to target location $j \in \{1, \ldots, N\}$, and equals zero otherwise.

Unlike modern RSL $\boldsymbol{y}_k$, pre-industrial RSL $\boldsymbol{Y}$ is modeled without residual autocorrelation in time. This choice is motivated by the nature of the RSL index points. Recall that we choose to infer $\boldsymbol{Y}$ only when and where RSL index points are available. This choice is made to speed up the algorithm. Index points at a particular saltmarsh are widely separated in time, typically by decades or centuries. Given these wide separation timescales, it is reasonable to assume that temporal autocorrelation between residual RSL values (deviations from the longterm trend) is negligible. The reasonableness of this assumption is corroborated by the residual analysis in the Supplementary Information. Were a longer time period considered, such that the dominant behavior is nonlinear, different choices would need to be made for modeling the pre-industrial RSL process.

Data level Given data from tide gauges at $M_k \leq N$ locations at time step k, we represent the data, $\boldsymbol{z}_k = [z_{1,k}, \ldots, z_{M_k,k}]^\mathsf{T}$, as gappy, noisy, and biased versions of the RSL process,

$$\boldsymbol{z}_k = \mathsf{H}_k \boldsymbol{y}_k + \boldsymbol{d}_k + \mathsf{F}_k \left(\boldsymbol{a} t_k + \boldsymbol{\ell} \right). \tag{8}$$

Here $\boldsymbol{d}_k$ is a random error sequence, cast as a temporally IID, spatially uncorrelated Gaussian field, $\boldsymbol{d}_k \sim \mathcal{N}\left(\mathbf{0}_{M_k}, \delta^2 \mathsf{I}_{M_k}\right)$, where δ^2 is a variance parameter. The site-specific data offsets $\boldsymbol{\ell}$ are modeled as a spatially uncorrelated normal random field, $\boldsymbol{\ell} \sim \mathcal{N}\left(\nu \mathbf{1}_M, \tau^2 \mathsf{I}_M\right)$, with mean ν and variance τ^2, where M is the total number of tide gauge sites ($N \geq M \geq M_k \; \forall k$). The data error trends $\boldsymbol{a}$ are also represented as a Gaussian random field without spatial correlation, $\boldsymbol{a} \sim \mathcal{N}\left(\mathbf{0}_M, \gamma^2 \mathsf{I}_M\right)$, where γ^2 is a variance parameter. Matrices H_k and F_k are selection matrices that isolate the process, data bias, and error trend vectors at the data sites at time step k.

Given GPS data at $L \leq N$ locations, we model the data, $\boldsymbol{x} = [x_1, \ldots, x_L]^\mathsf{T}$, as gappy, noisy versions of the underlying VLM process, $\boldsymbol{x} \sim \mathcal{N}\left(\mathsf{E}\boldsymbol{v}, \Delta\right)$. Here E is a selection matrix, which isolates the process at the observation sites, and Δ is an uncorrelated error covariance matrix, populated along the diagonal with error variances provided with the ULR 6a vertical velocity dataset. While Δ does not reflect uncertainties due to realization of an International Terrestrial Reference Frame, the impact of such systematic GPS data issues on the Bayesian inference can be gleaned from sensitivity experiments discussed in the Supplementary Information. It is because Δ is specified *a priori* that the nugget effect ε^2 is identifiable. Note that the data nugget effect ε^2 is distinct from the process variance parameter ϵ^2.

An important difference between tide gauge records and GPS data is that the former are spatiotemporal data (indexed in both space and time), whereas the latter are spatial data (indexed only in space). Whereas tide gauge records cover the period 1900–2017 (with at least one gauge returning data for each year of the epoch), GPS data only span the period 1995–2014, with many records covering only a fraction of that period. This poses a challenge from the perspective of inferring centennial rates of change. It is common to assume that VLM operates at steady rates over decades to centuries, and thus that GPS data are representative of much longer periods[25]. While not strictly true, this assumption is a useful approximation; standard errors of ~ 0.5 mm yr^{-1} are typical for 5-year GPS time series[41]. Our approach is to regard GPS data as a large-scale, long-period signal superimposed on small-scale, short-period noise. Our model is designed such that the signal is meant to be absorbed by the spatially structured field $\boldsymbol{u}$, whereas the noise is supposed to be captured by the spatially unstructured residual $\boldsymbol{v} - \boldsymbol{u}$. The underlying assumption is that large-scale, short-period and small-scale, long-period behaviors are negligible.

Given the RSL index points, we model the uncertain values of RSL, $\boldsymbol{Z} = [Z_1, \ldots, Z_{N_d}]^\mathsf{T}$, and age, $\boldsymbol{S} = [S_1, \ldots, S_{N_d}]^\mathsf{T}$, as noisy versions of the latent RSL values and their ages, $\boldsymbol{Z} \sim \mathcal{N}(\boldsymbol{Y}, \Gamma)$ and $\boldsymbol{S} \sim \mathcal{N}(\boldsymbol{T}, \Xi)$. Here Γ and Ξ are diagonal error covariance matrices, whose values are the formal error variances for the RSL and age estimates, respectively, provided with the Holocene RSL databases[4,12].

We select a set of $N = 211$ target locations, at which we make inference, to be the combined set of $M = 53$ tide gauge locations, $L = 42$ GPS stations, $N_s = 23$ saltmarshes, along with 93 regularly spaced $0.5° \times 0.5°$ grid points along the coast from southern Florida to northeastern

Maine where no observations are present (Fig. 1a–1d).

Prior level To close the model, we place proper, mostly conjugate[42] priors on the model parameters. Generally, these priors are selected to be diffuse, such that they have little influence on the posterior (see Supplementary Information). However, there are some exceptions that are important for understanding the results in the main text.

Given our interest in large-scale processes (variable ocean dynamics, melting of ice sheets, etc.), we condition the inference by constraining the inverse range parameters ϕ, ρ, and λ in equations (2), (5), and (6) such that corresponding length scales characterizing the spatially correlated RSL innovations $\boldsymbol{e}_k$, and trends in VLM $\boldsymbol{u}'$ and SSH $\boldsymbol{w}'$ unrelated to GIA have 95% prior probability of falling between roughly 500 and 2,000 km. However, posterior solutions are robust to such details of prior selection; nearly identical posterior solutions for regional trend vectors are produced if wider or narrower priors are used on these parameters to condition the inference to focus on large scales of interest to geology and climate (see Supplementary Information). Moreover, past authors note that providing a prior sense of spatial scale on the inverse range is sometimes necessary to ensure convergence of the algorithm used to draw samples from the posterior distribution[17,43–47].

Given our particular interest in GIA, we place informative priors on the VLM and SSH trend vectors $\boldsymbol{u}_g$ and $\boldsymbol{w}_g$ related to GIA. Specifically, we place multivariate normal priors on these fields, with mean vectors and covariance matrices defined based on the 216 GIA model predictions. See the Supplementary Information for more details.

Drawing samples from the posterior distribution Using Bayes' rule, the process and data level equations (1–8), and the priors, we assume that the posterior probability distribution of the process and parameters given the available data breaks down as

$$\begin{aligned} p\left(\boldsymbol{y}, \boldsymbol{Y}, \boldsymbol{T}, \Theta | \boldsymbol{x}, \boldsymbol{z}, \boldsymbol{Z}, \boldsymbol{S}\right) \;&\propto\; p\left(\boldsymbol{x}, \boldsymbol{z}, \boldsymbol{Z}, \boldsymbol{S} | \boldsymbol{y}, \boldsymbol{Y}, \boldsymbol{T}, \Theta\right) \cdot p\left(\boldsymbol{y}, \boldsymbol{Y}, \boldsymbol{T}, \Theta\right), \qquad (9) \\ &= p\left(\boldsymbol{y}_0\right) \cdot p\left(r\right) \cdot p\left(\sigma^2\right) \cdot p\left(\phi\right) \cdot p\left(\mu\right) \cdot p\left(\pi^2\right) \cdot p\left(\lambda\right) \cdot p\left(\alpha\right) \\ &\cdot\; p\left(\omega^2\right) \cdot p\left(\rho\right) \cdot p\left(\varepsilon^2\right) \cdot p\left(\delta^2\right) \cdot p\left(\nu\right) \cdot p\left(\tau^2\right) \cdot p\left(\gamma^2\right) \cdot p\left(\beta\right) \\ &\cdot\; p\left(\kappa^2\right) \cdot p\left(\epsilon^2\right) \cdot p\left(\boldsymbol{w}_g\right) \cdot p\left(\boldsymbol{u}_g\right) \cdot p\left(\boldsymbol{b} | \boldsymbol{u}, \boldsymbol{w}_g, \mu, \pi^2, \lambda\right) \\ &\cdot\; p\left(\boldsymbol{u} | \boldsymbol{u}_g, \alpha, \omega^2, \rho\right) \cdot p\left(\boldsymbol{v} | \boldsymbol{u}, \varepsilon^2\right) \cdot p\left(\boldsymbol{\ell} | \nu, \tau^2\right) \cdot p\left(\boldsymbol{a} | \gamma^2\right) \\ &\cdot\; p\left(\boldsymbol{x} | \boldsymbol{v}\right) \cdot p\left(\boldsymbol{\iota} | \beta, \kappa^2\right) \cdot p\left(\boldsymbol{Y} | \boldsymbol{u}_g, \boldsymbol{w}_g, \boldsymbol{T}, \boldsymbol{\iota}, \epsilon^2\right) \cdot p\left(\boldsymbol{Z} | \boldsymbol{Y}\right) \cdot p\left(\boldsymbol{S} | \boldsymbol{T}\right) \\ &\cdot\; \prod_{k=1}^{K} \left[p\left(\boldsymbol{z}_k | \boldsymbol{y}_k, \delta^2, \boldsymbol{\ell}, \boldsymbol{a}\right) \cdot p\left(\boldsymbol{y}_k | \boldsymbol{y}_{k-1}, \boldsymbol{b}, r, \sigma^2, \phi\right) \right]. \end{aligned}$$

Here p is probability density, $|$ is conditionality, $\propto$ is proportionality, and $\Theta \doteq \{\boldsymbol{b}, \boldsymbol{u}, \boldsymbol{w}, \dots\}$ is the set of all model parameters. Above, we assume that the data are conditionally independent given the process and the parameters.

We draw samples from the posterior distribution using Markov chain Monte Carlo (MCMC) methods similar to Piecuch et al.[17]. We evaluate full conditional distributions for using a Gibbs sampler, with Metropolis steps use for the inverse range parameters. We perform 400,000 MCMC iterations, setting the initial process values to zero, and randomly drawing initial parameter values from the priors. We discard the first 200,000 draws to eliminate initialization transients, and keep only 1 out of every 200 samples to reduce the impacts of serial correlation between draws. Convergence is evaluated by comparing variance between and within chains. Results are based on 3 such 1,000-member chains concatenated together.

33. Permanent Service for Mean Sea Level (PSMSL). Tide Gauge Data, Retrieved 24 May 2018 (2018) [Available at http://www.psmsl.org/data/obtaining/].

34. Altamimi, Z., X. Collilieux, & L. Métivier. ITRF2008: an improved solution of the international terrestrial reference frame, *J. Geodesy*, **85**, 8, 457–473 (2011).

35. Engelhart, S.E., B. P. Horton, & A. C. Kemp. Holocene sea level changes along the United States' Atlantic Coast, *Oceanography*, **24**, 2, 70–79 (2011).

36. Bos, M. S., S. D. P. Williams, I. B. Araújo, & L. Bastos. The effect of temporal correlated noise on the sea level rate and acceleration uncertainty, *Geophys. J. Int.*, **196**, 1423–1430 (2014).

37. Banerjee, S., B. P. Carlin, & A. E. Gelfand. *Hierarchical Modeling and Analysis for Spatial Data*, 448 pp., Chapman and Hall, Boca Raton (2004).

38. Woodworth, P. L., M. A. Morales Maqueda, V. M. Roussenov, R. G. Williams, & C. W. Hughes. Mean sea-level variability along the northeast American Atlantic coast and the roles of the wind and the overturning circulation, *J. Geophys. Res. Oceans*, **119**, 8916–8935, doi:10.1002/2014JC010520 (2014).

39. Thompson, P. R., & G. T. Mitchum. Coherent sea level variability on the North Atlantic western boundary, *J. Geophys. Res. Oceans*, **119**, 5676–5689, doi:10.1002/2014JC009999 (2014).

40. Piecuch, C. G., S. Dangendorf, R. M. Ponte, & M. Marcos. Annual sea level changes on the North American Northeast Coast: Influence of local winds and barotropic motions, *J. Clim.*, **29**, 4801–4816 (2016).

41. Santamaría-Gómez, A., and A. Mémin. Geodetic secular velocity errors due to interannual surface loading deformation, *Geophys. J. Int*, **202**, 763–767 (2015).

42. Gelman, A., J. B. Carlin, H. S. Stern, & D. B. Rubin. *Bayesian Data Analysis, 2nd ed.*, 668 pp., Chapman and Hall, Boca Raton (2004).

43. Zhang, H. Inconsistent Estimation and Asymptotically Equal Interpolations in Model-Based Geostatistics, *J. Am. Stat. Assoc.*, **99**, 465, 250–261, doi:10.1198/016214504000000241 (2004).

44. Tingley, M. P., & P. Huybers. A Bayesian algorithm for reconstructing climate anomalies in space and time. Part I: Development and applications to paleoclimate reconstruction problems, *J. Clim.*, **23**, 2759–2781 (2010).

45. Mannshardt, E., P. F. Craigmile, & M. P. Tingley. Statistical modeling of extreme value behavior in North American tree-ring density series, *Clim. Change*, 117, 843–858, doi:10.1007/s10584-012-0575-5 (2013).

46. Tierney, J. E., & M. P. Tingley. A Bayesian, spatially-varying calibration model for the TEX_{86} proxy, *Geochim. Cosmochim. Ac.*, **127**, 83–106 (2014).

47. Werner, J. P., & M. P. Tingley. Technical Note: Probabilistically constrained proxy age-depth models within a Bayesian hierarchical reconstruction model, *Clim. Past*, **11**, 533–545, doi:10.5194/cp-11-533-2015 (2015).

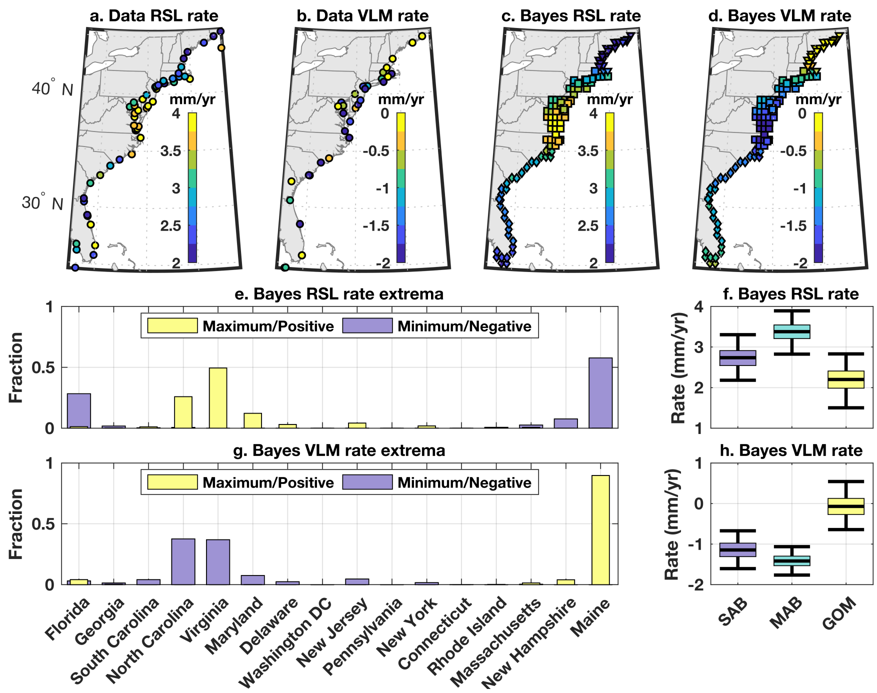
a. Data RSL rate
b. Data VLM rate
c. Bayes RSL rate
d. Bayes VLM rate
40° N
30° N
mm/yr
e. Bayes RSL rate extrema
Maximum/Positive
Minimum/Negative
Fraction
f. Bayes RSL rate
Rate (mm/yr)
g. Bayes VLM rate extrema
h. Bayes VLM rate
Florida
Georgia
South Carolina
North Carolina
Virginia
Maryland
Delaware
Washington DC
New Jersey
Pennsylvania
New York
Connecticut
Rhode Island
Massachusetts
New Hampshire
Maine
SAB
MAB
GOM

[Figure 1]

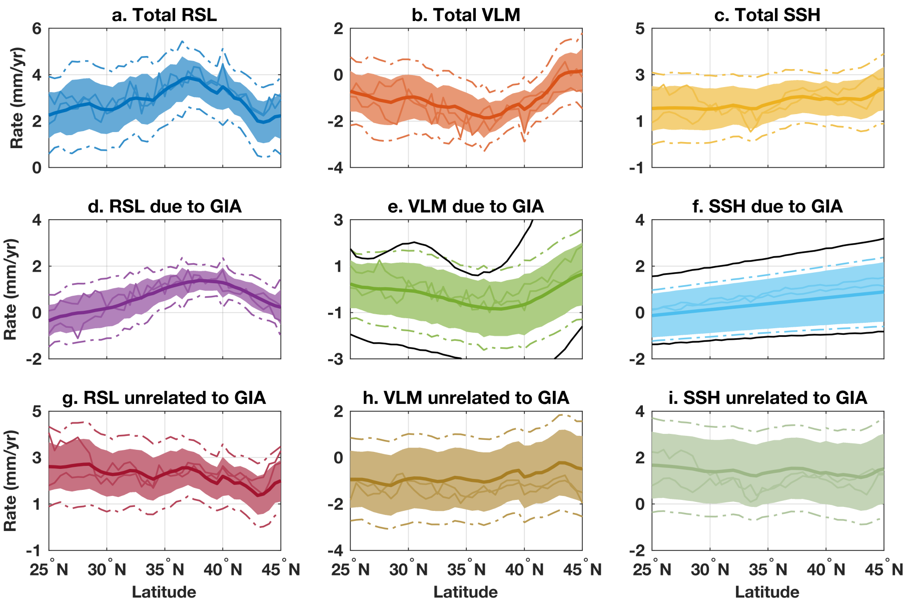
a. Total RSL
b. Total VLM
c. Total SSH
d. RSL due to GIA
e. VLM due to GIA
f. SSH due to GIA
g. RSL unrelated to GIA
h. VLM unrelated to GIA
i. SSH unrelated to GIA
Rate (mm/yr)
25°N 30°N 35°N 40°N 45°N
Latitude

[Figure 2]

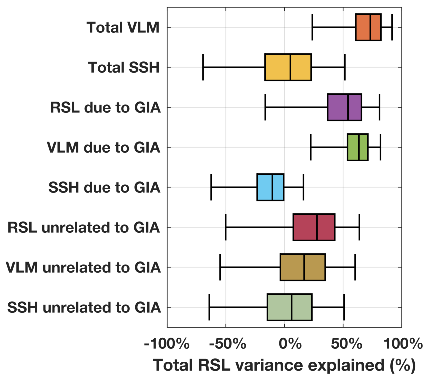
Total VLM
Total SSH
RSL due to GIA
VLM due to GIA
SSH due to GIA
RSL unrelated to GIA
VLM unrelated to GIA
SSH unrelated to GIA
-100%
-50%
0%
50%
100%
Total RSL variance explained (%)

487 [Figure 3]

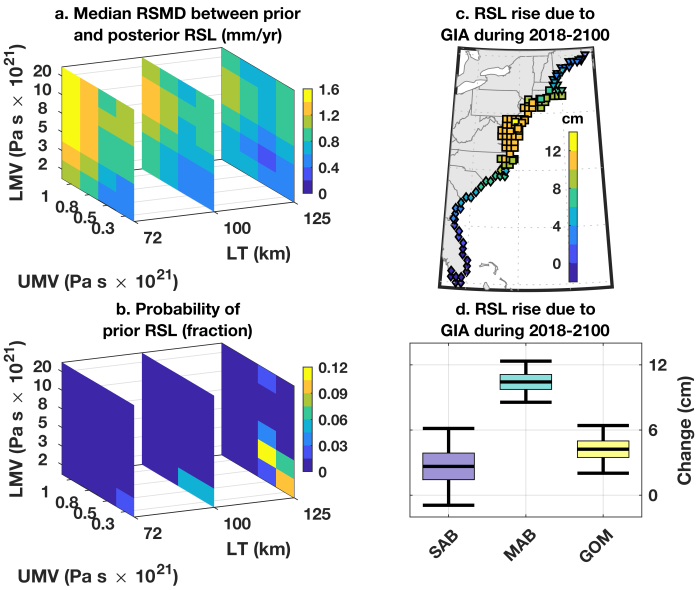

a. Median RSMD between prior
and posterior RSL (mm/yr)
LMV (Pa s × 10^21)
UMV (Pa s × 10^21)
LT (km)
c. RSL rise due to
GIA during 2018-2100
cm
b. Probability of
prior RSL (fraction)
d. RSL rise due to
GIA during 2018-2100
Change (cm)
SAB
MAB
GOM

488 [Figure 4]

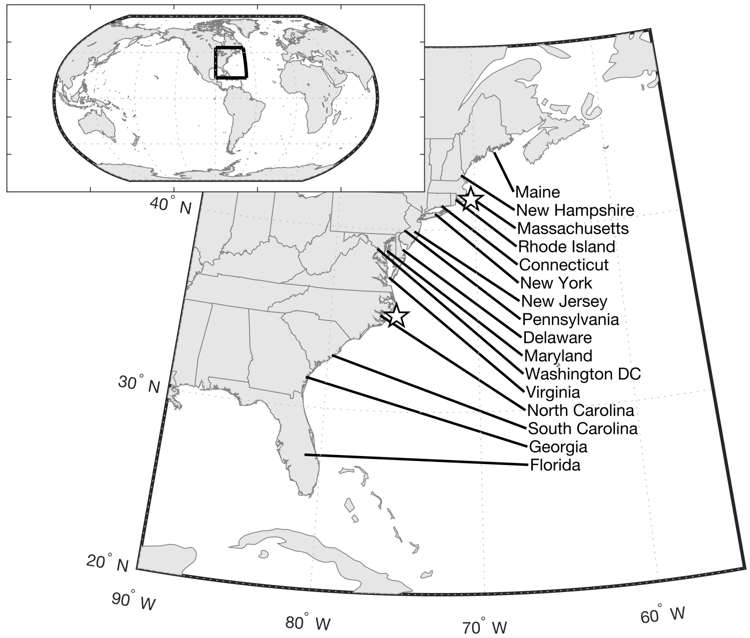

[Extended Data Figure 1]

Figure 1 **Rates of change. a–b,** Trends in (**a**) tide gauge RSL and (**b**) GPS station VLM. **c–d,** Median modeled (**c**) RSL and (**d**) VLM trends. Diamonds indicate South Atlantic Bight (SAB), boxes Mid-Atlantic Bight (MAB), triangles Gulf of Maine (GOM). **e, g,** Modeled probability that maximum/most-positive or minimum/most-negative (**e**) RSL and (**g**) VLM trend occurred in a given state. **f, h,** Model medians (lines), interquartile ranges (shading), and 95% credible intervals (whiskers) on SAB-, MAB-, and GOM-averaged (**f**) RSL and (**h**) VLM trends.

Figure 2 **Latitudinal structure. a–i,** Posterior median (thick line), 95% pointwise (light shade) and pathwise (thin dash) credible intervals, and two sample draws from the model solution (thin lines) for regional trends versus latitude for (**a**), RSL, (**b**), VLM, (**c**), SSH, (**d**), GIA-driven RSL, (**e**), GIA-driven VLM, (**f**), GIA-driven SSH, (**g**), non-GIA RSL, (**h**), non-GIA VLM, and (**i**), and non-GIA SSH. The 95% pathwise credible interval are determined by broadening the 95% pointwise credible intervals until 95% of the solutions are encompassed. Black lines are prior 95% pointwise credible intervals.

Figure 3 **Contributions to spatial differences.** Model median (black vertical lines), interquartile range (color shading), and 95% credible interval (black whiskers) for the alongshore spatial variance in regional RSL linear trends during 1900–2017 explained by VLM or SSH related to GIA or other processes. Percentage variance V in x explained by y is defined as $100\% \times [1 - \mathrm{var}(x-y)/\mathrm{var}(x)]$, where var is variance. Given the differences in sign convention (e.g., a negative VLM rate corresponds to positive RSL trend), variances explained in RSL by VLM terms are computed by adding, rather than subtracting, the respective VLM component.

Figure 4 **GIA-driven RSL trends.** **a,** Median root-mean-square deviation between prior and posterior GIA-driven RSL trends as a function of rheological parameters used for the priors: lithospheric thickness (LT), upper-mantle viscosity (UMV), and lower-mantle viscosity (LMV). **b,** Marginal posterior probability distribution that best correspondence between prior and posterior solutions occurs for a given combination of rheological parameters. **c,** Posterior medians of large-scale GIA-driven RSL change along the coast during 2018–2100. **d,** Posterior medians (lines), interquartile ranges (shading), and 95% credible intervals (whiskers) on the GIA-driven RSL rise during 2018-2100 averaged over the SAB, MAB, and GOM.

Figure 5 Extended Data Figure 1 **Study region.** Map of the U.S. East Coast and individual coastal states. Two white stars indicate Cape Cod (north) and Cape Hatteras (south), demarcating the three study regions: Gulf of Maine, Mid-Atlantic Bight, and South Atlantic Bight.